Electron momentum density studies in high-T_c materials by positron annihilation spectroscopy: theory and experiment

1990 J. Phys.: Condens. Matter 2 1635

(http://iopscience.iop.org/0953-8984/2/6/021)

J. Phys.: Condens. Matter **2** (1990) 1635–1658. Printed in the UK

Electron momentum density studies in high-T_c materials by positron annihilation spectroscopy: theory and experiment

P E A Turchi†, A L Wachs†, K H Wetzler†, J H Kaiser‡, R N West§, Y C Jean†§, R H Howell† and M J Fluss†

† Lawrence Livermore National Laboratory (L-268), PO Box 808, Livermore, CA 94550, USA

‡ University of Texas-Arlington, Arlington, TX 76019, USA

Received 14 February 1989, in final form 12 June 1989

Abstract. We discuss positron behaviour and in particular the ground state positron probability in high-T_c materials. Special attention is paid to La_2CuO_4, for which we report detailed high-resolution two-dimensional angular correlation of positron annihilation radiation spectroscopy measurements in three sample orientations and as a function of temperature. Besides a large isotropic core-like electron contribution ($\simeq 85\%$), the remaining anisotropic contribution is attributed to valence electrons which are modelled by a linear combination of atomic orbitals–molecular orbital method in conjunction with a localised ion scheme, within the independent particle model approximation. The covalency structure so derived is used to discuss the case of the parent doped material and $YBa_2Cu_3O_7$. We also comment on the application of the Lock–Crisp–West theorem to La_2CuO_4, before adding some concluding remarks.

1. Introduction

Since the renewal of interest for the oxometallate compounds [1, 2] after the discovery of high-T_c superconducting properties in $La_{2-x}Sr_xCuO_4$ by Bednorz and Müller [3], and subsequently in $YBa_2Cu_3O_{7-y}$ by Wu *et al* [4], intensive experimental and theoretical studies have been undertaken to clarify the chemistry as well as the physics of these materials. Despite the large variety of models invoked to explain the superconducting mechanism, there is currently a consensus to admit the major role played by the intrinsic electronic structure in these oxides. This key ingredient has been primarily investigated theoretically by making use of various one-electron band theories (APW, LMTO, ASW . . .) [5]. These calculations in turn initiated a number of photoemission studies to check the validity of such approaches [6].

In the present paper, we will start from the opposite viewpoint, according to which valence electrons are supposed to be correlated so strongly that they preferably form localised states rather than itinerant Bloch states. Hence, starting from an ionic picture and allowing covalency overlap to take place, the linear combination of atomic orbital–

§ Permanent address: University of Missouri-Kansas, Kansas City, MO 64110, USA.

0953-8984/90/061635 + 24 $03.50

molecular orbital model (LCAO-MO) constitutes a qualitatively appropriate framework to describe the electronic structure.

Among the experimental techniques pertaining to such an approach, positron annihilation spectroscopy (PAS) is known to be suitable for probing the electronic structure and defects in solids. The recent results of lifetime measurements have also proved the sensitivity of the positron (e^+) to superconductivity in these high-T_c materials [7, 8]. In order to gain more insight into the physics involved in the annihilation process, high-resolution two-dimensional angular correlation of positron annihilation radiation (2D ACPAR) studies are highly desirable. The recent improvements in the 2D ACPAR detection systems, and particularly in the instrumental resolution, have led to information about the electron momentum densities in pure metals, ordered intermetallic compounds [9] as well as in disordered alloys [10], with an accuracy which greatly compares to the de Haas–van Alphen results in the case of periodic systems.

Recent 2D ACPAR experiments performed on a nearly defect-free single crystal of La_2CuO_4 [11] show:

(i) no discernible structure at the Brillouin zone boundaries and highly isotropic angular correlation spectra for various crystalline orientations, as already reported for other oxides such as NiO [12];

(ii) well defined residual anisotropies in the positron–electron 2γ annihilation angular correlation curves along various directions.

The purpose of this paper is twofold: first, to prove that the positron is suitable for probing the copper–oxygen bonds which are supposedly responsible for the high-T_c superconductivity; and second, to relate the 2D ACPAR data to particular details of the electronic structure of La_2CuO_4. Since this material represents a base line for future studies of the Fermi surface topology we have applied the well known Lock–Crisp–West (LCW) theorem to analyse the data in the context of the obvious other extreme assumption, namely a band-theoretical interpretation. We will comment *in fine* on the expected behaviour of the positron in the doped material $La_{2-x}Sr_xCuO_4$ and the parent defected $YBa_2Cu_3O_{7-y}$.

The paper is organised as follows. In § 2, we define the positron wavefunction in these systems; in § 3, we report the experimental results of high-resolution 2D ACPAR measurements performed on a nearly defect-free La_2CuO_4 single crystal in three crystallogrphic orientations and as a function of temperature; in § 4, we first discuss the LCAO-MO model that is used in conjunction with a localised ion scheme within the independent particle model (IPM) approximation to calculate the momentum distribution of annihilating electron–positron pairs; then detailed comparisons between theory and experiment are presented in terms of covalency overlap parameters describing the mixing of 3d copper orbitals with 2s and 2p oxygen orbitals. In § 5 we apply the Lock–Crisp–West folding procedure which allows a more direct connection with electron momentum density in reciprocal space, and in § 6 we briefly examine the consequences of our approach on the effect of a dopant in La_2CuO_4 and what can be expected for $YBa_2Cu_3O_{7-y}$.

2. Positron wavefunction

Since the positron annihilation rate is an overlap integral between the wavefunctions of the electrons and the positron at the same location, we need first to obtain the positron

Table 1. Crystallographic information (in a.u.) and α parameters of the positron wavefunction for La_2CuO_4, $La_{1.85}Sr_{0.15}CuO_4$ and $YBa_2Cu_3O_7$.

La_2CuO_4 [16]	$La_{1.85}Sr_{0.15}CuO_4$ [46]	$YBa_2Cu_3O_7$ [17]
$a = 7.2040$	$a = 7.1418$	$a = 7.3333$
		$b = 7.2052$
$c = 24.9021$	$c = 24.9935$	$c = 21.9781$
d(Cu–O1) = 3.6020	d(Cu–O1) = 3.5709	d(Cu–O1) = 3.6661
d(Cu–O2) = 4.5322	d(Cu–O2) = 4.5588	d(Cu–O4) = 3.5064
$\alpha_0 = 1.437$	$\alpha_0 = 1.419$	$\alpha_{O4} = 1.329$
$\alpha_{Cu} = 0.647$	$\alpha_{Cu} = 0.640$	$\alpha_{O1\text{-}O3} = 1.326$
$\alpha_{La} = 0.253$	$\alpha_{Sr} = 0.370$	$\alpha_{Cu1} = 0.605$
	$\alpha_{La} = 0.250$	$\alpha_{Cu2} = 0.602$
		$\alpha_Y = 0.353$
		$\alpha_{Ba} = 0.229$

density distribution in order to find the preferential positions of the positron in these materials. As is usually assumed, the thermalised positron will be taken in a ground state with zero momentum (at $T = 0$ K) and a complete $l = 0$ character. If we exclude any trapping of the positron by negative ions, i.e. no quasiatomic state of the e^+–anion type, an assumption which is corroborated by the lifetime measurement results [7], the e^+ will be considered in a Bloch state. As was suggested by Chiba [12, 13], the positron wavefunction $\Psi^+(r)$ can be approximated by a variational function which properly takes into account the fairly localised electronic character of the material and also the relative affinities of the different species to the positron in the annihilation process. Following reference [13], the trial function $\Psi^+(r)$ is written as

$$\Psi^+(r) = N^{-1/2}\left[1 - \sum_\nu \exp(-\alpha_\nu |\boldsymbol{r} - \boldsymbol{R}_\nu|^2\right]$$

where the set of α_ν represents the variational parameters to be determined, N is a normalisation constant and $\boldsymbol{R}_\nu$ describes one of the set of coordinates of the inequivalent sites ν in the unit cell.

This function is associated with the Hamiltonian

$$H^+ = -\Delta/2 + V \qquad V = \sum_\nu v(|\boldsymbol{r} - \boldsymbol{R}_\nu|)$$

where V is a sum of non-overlapping atomic potentials centred around $\boldsymbol{R}_\nu$. Each potential is given by the Coulomb part of the electron potential, with a negative sign, from which the exchange-correlation part is omitted. These potentials can be calculated from the Herman–Skillman neutral atomic charge distributions of the different atoms [14], as far as the Madelung potential (acting repulsively to a positron) is largely cancelled out by the attractive potential in the negative ion region [15]. (Atomic units are used throughout the text.)

From the expectation value of the energy, the α_ν are variationally deduced by solving a set of non-linear integral equations [13]. It is anticipated that the larger the ionic core is, the stronger it acts as a repulsive centre for the positron and therefore the smaller the value of α_ν is. As an illustration of the method, the α_ν, given in table 1, were calculated for La_2CuO_4 and $YBa_2Cu_3O_7$, with the structural information of Longo and Raccah [16]

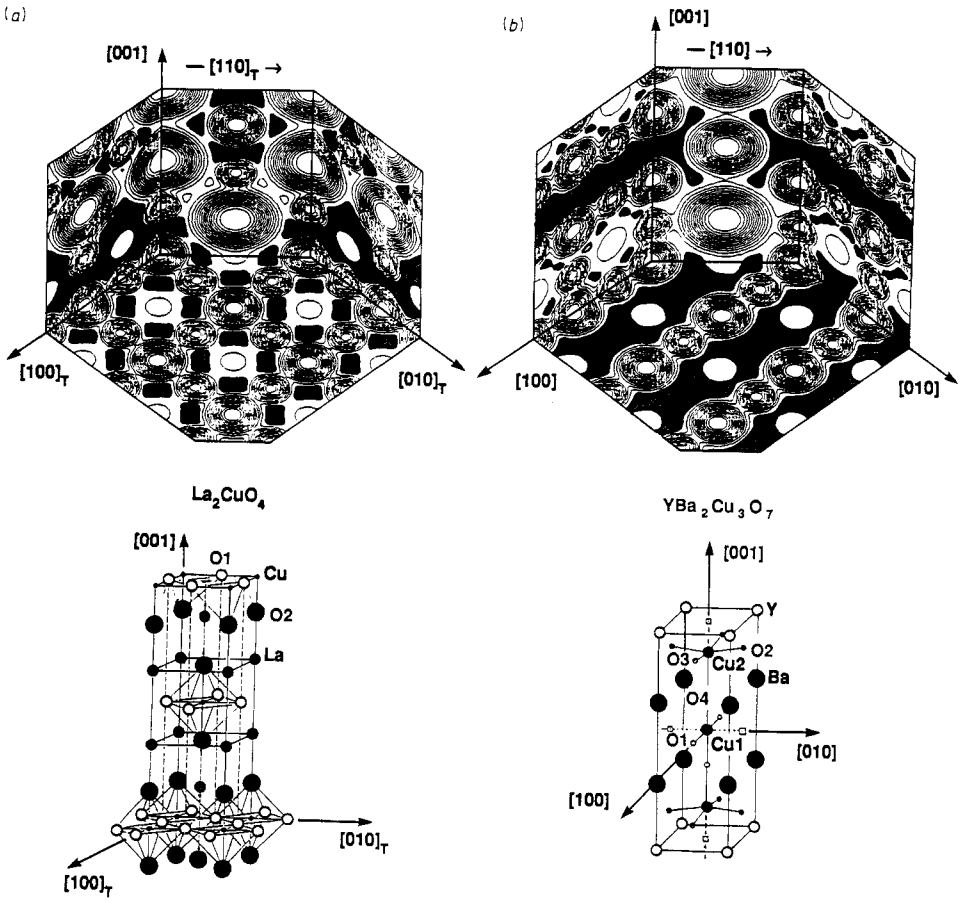

Figure 1. Isodensity contour plots of the positron probability in various planes of: (*a*) La_2CuO_4; (*b*) $YBa_2Cu_3O_7$. The highlighted regions correspond to the highest probability.

and Capponi *et al* [17] respectively. In figures 1(*a*) and (*b*) the positron iso-density contour distribution maps $|\Psi^+(r)|^2$ are represented for both perovskites in various planes.† The similarity in the nature of the spatial distribution of the positron in the two oxides can be described by imagining the positron as wrapped about the Cu–O1 and Cu–O2 bonds in La_2CuO_4 and as preferentially located near the Cu1–O1 and Cu1–O4 bonds in $YBa_2Cu_3O_7$, keeping in mind the location of the maximum electronic charge distribution in order for the annihilation process to take place. From figures 1(*a*) and (*b*), it appears that PAS is well adapted to characterise the electronic properties of this part of these materials which are supposed to be responsible for the superconductivity properties. One can notice that a qualitative agreement with LAPW results [18] for the positron charge density in $YBa_2Cu_3O_7$ (where no electron–positron correlation effects [19] have been included) is achieved.

† For simplicity the La_2CuO_4 structure is assumed to be base-centred tetragonal; i.e. the Cu–O octahedral tilting and the departure from a square planar basal configuration of oxygen atoms, which are responsible for the orthorhombic symmetry of the oxide lattice below 533 K, are neglected.

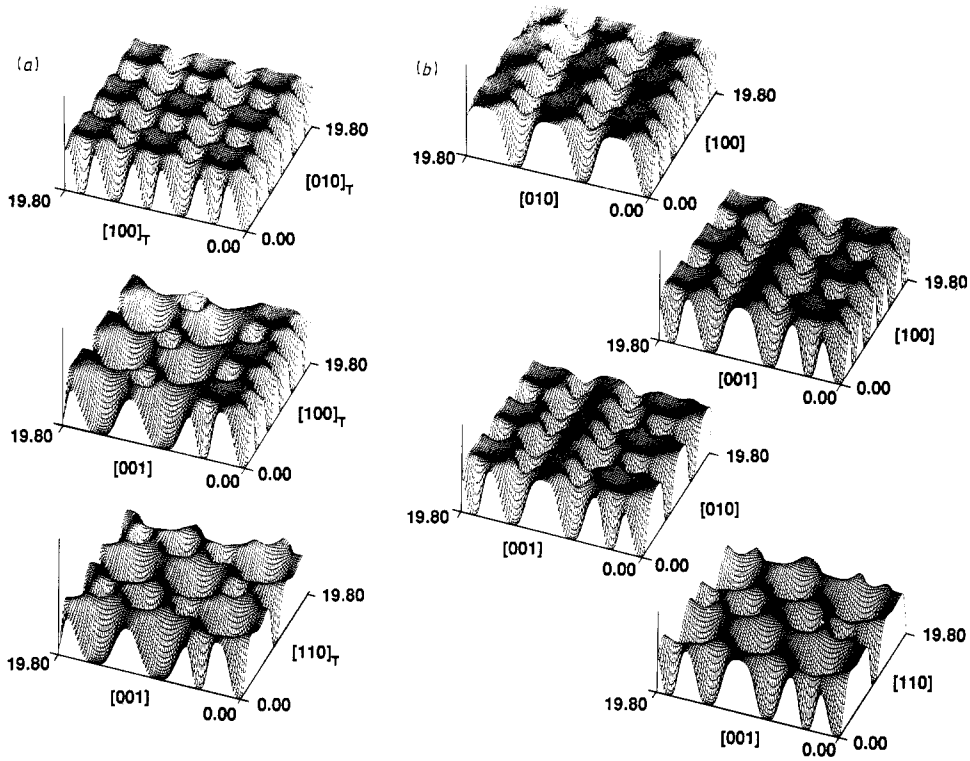

Figure 2. Positron probability densities for: (*a*) La_2CuO_4 (in the {001}, {010} and {110} planes); (*b*) $YBa_2Cu_3O_7$ (in the {001}, {010}, {100} and {110} planes). Distances are expressed in a.u.

In figures 2(*a*) and (*b*), three-dimensional plots of the positron probability density in various planes further illustrate the regions of free volume occupied by the positron in La_2CuO_4 and $YBa_2Cu_3O_7$ respectively. In both oxides, the cations (La, Ba and to a lesser extent Y) force the positron to probe the copper–oxygen bonds more selectively. Hence, in the defect-free $YBa_2Cu_3O_7$ oxide, it is unlikely that the positron will trap in the $\square_y$ (along the *b* axis) or $\square_z$ (along the *c* axis) vacancy sites. It is worth noting that the existence of additional vacancy sites (divacancies or cluster of vacancies) will act more effectively as trapping centres for the positron, particularly those in the O1 position where the negative charge left by the missing oxygen will overcome the repulsion effect caused by the four surrounding barium atoms. Such an effect might explain the apparent contradiction in the positron lifetime measurements performed on these perovskites: the intermediate lifetime of 210 ps [7] in the defected system could be attributed to the large number of trapping sites (eventually clusters of oxygen vacancies), whereas the bulk lifetime of 176 ps [7] would be characteristic of a delocalised positron.

3. Electron–positron annihilation in La_2CuO_4: experimental results

We have measured the electron–positron annihilation momentum density in La_2CuO_4 using two-dimensional angular correlation of positron annihilation radiation (ACPAR)

techniques. ACPAR has been used most successfully in clarifying the Fermi surfaces of metals [9], ordered compounds, and disordered alloys [10]. Limited studies have been performed on oxides [12, 13, 20–26], most notably NiO [12], Fe_3O_4 [13, 20], $Na_{0.64}WO_3$ [23] and recent preliminary work on La_2CuO_4 [11, 25] and $YBa_2Cu_3O_7$ [26, 27].

The ACPAR experiments were made with the new 2D ACPAR facility at the Lawrence Livermore National Laboratory. Briefly, the apparatus consists of two General Electric Medical Systems 'Starport' Anger cameras modified to function as coincidence positron annihilation γ-ray counters. Position and energy data of coincidence γ-rays are selected and digitised by dedicated, stand-alone microprocessors and sorted online by a Micro-Vax II computer. We estimate the overall momentum resolution to be 0.5×10^{-3} mc (= 0.5 mrad).

The La_2CuO_4 crystals were grown from a PbO-based flux with the *c* axis perpendicular to the growth faces. Subsequent x-ray difraction measurements showed significant microtwinning in the near-surface ($\sim 100\ \mu$m) region. Magnetoresistance and susceptibility measurements made on equivalent crystals indicated no evidence of antiferromagnetic ordering or superconductivity above 1.8 K [28]. Two such crystals of dimensions $\sim 4 \times 4 \times 2\ mm^3$ were oriented in approximate (orthorhombic) registry, 'sandwiched' about a ~2 mCi encapsulated ^{22}Na point source in ~1 μm polycrystalline Ni foil ($\sim 1.1\ mg\ cm^{-2}$), and sealed in an Al cell under an ultrahigh-purity ^4He atmosphere for the duration of the experiment. The cell in turn was mounted in a closed-cycle He refrigeration system where it would be cooled to as low as 8 K with an accuracy of ±0.1 K.

The positron annihilation lifetime was measured initially to assure that there was no detectable trapping of the positron which would obviate the interpretation of the ACPAR data in terms of a single positron wavefunction [11]. The apparatus used for these measurements has been described elsewhere [7]. Approximately 10^6 counts were accumulated in each of three lifetime measurements at room temperature. All of the results showed only two lifetime components. The longer one, of 0.46 ns and intensity 4%, is attributed to surface and source annihilation of Ps and positrons. No more than one remaining lifetime could be resolved from the data. On the basis of these results, it was concluded [11] that only a single bulk lifetime, 177 ± 1 ps, exists in La_2CuO_4 and vacancy trapping is negligible. This result is in agreement with similar measurements on $La_{1.85}Sr_{0.15}CuO_4$ reported by Jean *et al* [7].

Two-dimensional ACPAR measurements were performed on the samples at 9 K, 70 K and room temperature (298 K) for the positron–electron momentum integration direction along the *c* axis (perpendicular to the basal plane), at 9 K and at room temperature for the integration direction along a principal twinning axis of the basal plane, and at room temperature only for integration along the *a* axis of the samples when referred to a tetragonal cell. All of the sample detector geometries are illustrated schematically (see below). The detectors and the sample were separated by 9.6 m. A typical measurement consisted of 16 to 40 million coincidence annihilation counts.

Figure 3 shows a representative two-dimensional electron–positron momentum distribution obtained with the integration direction perpendicular to the indicated tetragonal crystalline axes. The inset shows the orientation of the integration axis with respect to the La_2CuO_4 unit cell. The distribution is broad and highly isotropic, but has small anisotropic deviations. The measured momentum distributions for the other two integration directions are qualitatively similar.

Broad, highly isotropic and nearly featureless electron–positron momentum distributions are characteristic findings for ACPAR measurements of covalent metal oxides.

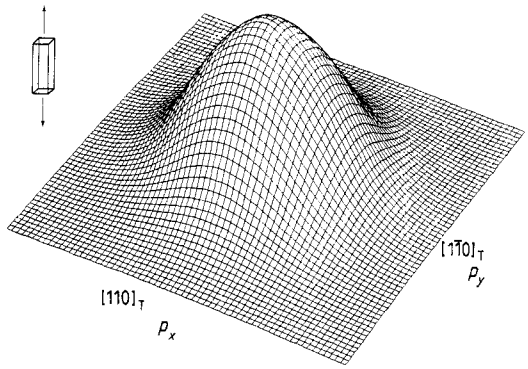

Figure 3. Two-dimensional electron–positron momentum distribution of La_2CuO_4 with a momentum direction of integration along the c axis of the sample, at room temperature. The inset shows the associated sample geometry. The values of p_x and p_y between -13.1 and $+13.1 \times 10^{-3}$ mc.

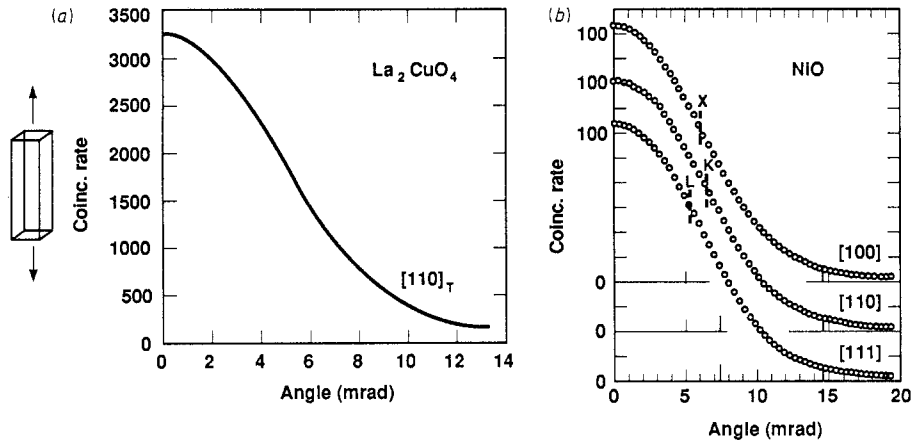

Figure 4. (*a*) One-dimensional electron–positron momentum distribution of La_2CuO_4, obtained after projection onto the [100] axis. (*b*) The angular correlations of NiO along [100], [110] and [111] directions (from [12]) are also displayed for comparison.

In figure 4 we display the spectrum of figure 3 projected onto the [110] tetragonal axis (full curve), and the one-dimensional ACPAR data for NiO [12]. There are no discernible structures corresponding to the existence of a Fermi surface or Brillouin zone boundaries in either of the two curves.

The anisotropic features are extracted from the underlying isotropic distributions for each of the three momentum integration directions by subtracting annular averaged reference values from each distribution. Residual anisotropy surfaces for each geometry were then signal-averaged using the point group symmetry of the crystal with respect to the integration axis and further smoothed to reduce the signal to noise ratio. The results of these operations are shown in figures 5(*a*), (*b*) and (*c*). We also display iso-density plots of the corresponding residual anisotropy surfaces and schematically illustrates each integration geometry. The effective resolution is $\sim 0.75 \times 10^{-3}$ mc.

The significant results of the low-temperature measurements are shown in figures 6, 7 and 8. Figure 6(*a*) shows the residual anisotropy surface for the [001] axis integration

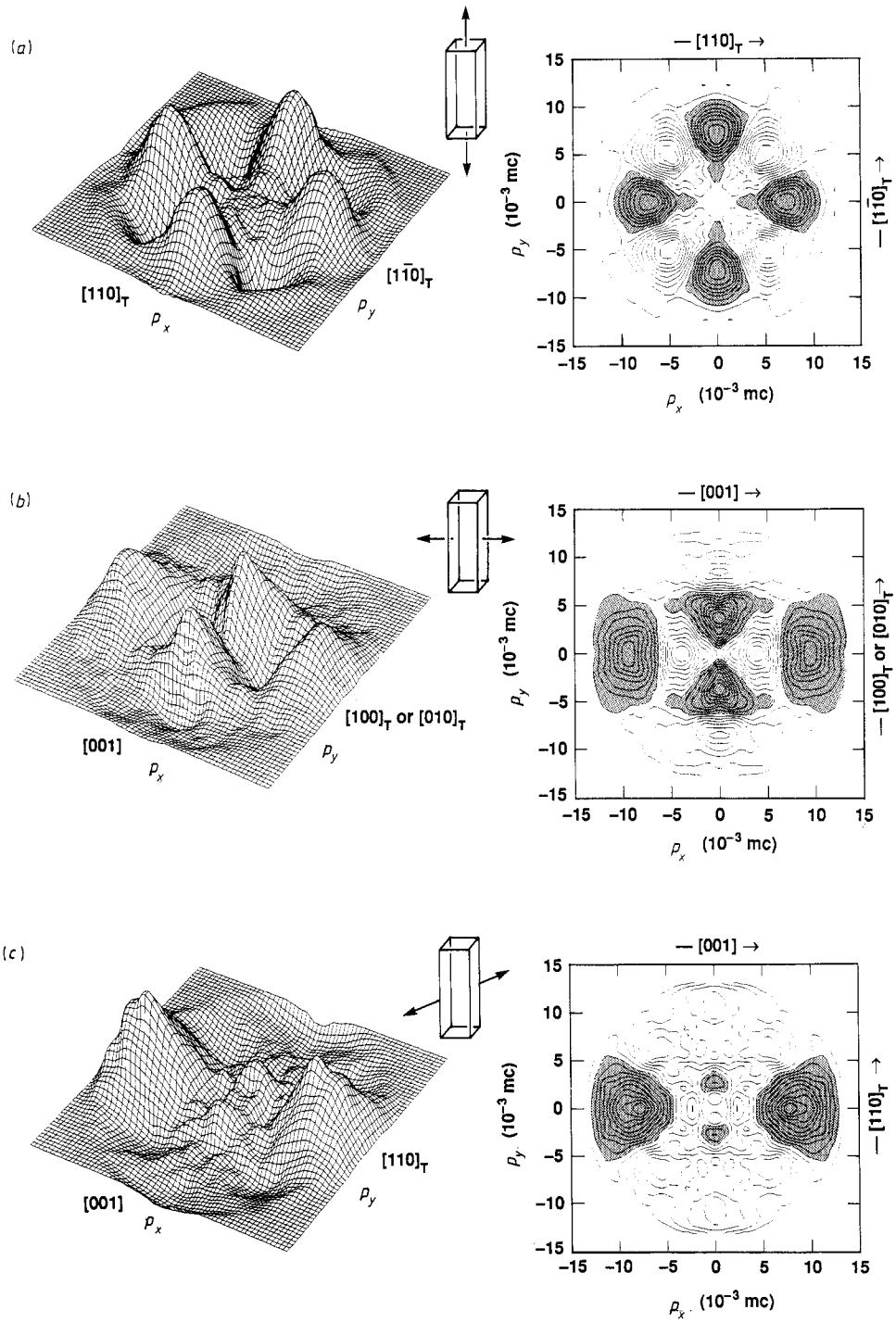

Figure 5. Experimental 3D residual aniosotropy surfaces of the electron–positron annihilation momentum distributions of La_2CuO_4 with momentum integration direction along the indicated crystalline axis (data taken at room temperature). The insets show the integration directions with respect to the sample geometries. The corresponding isodensity plots are also displayed (contour zone above the average have been highlighted).

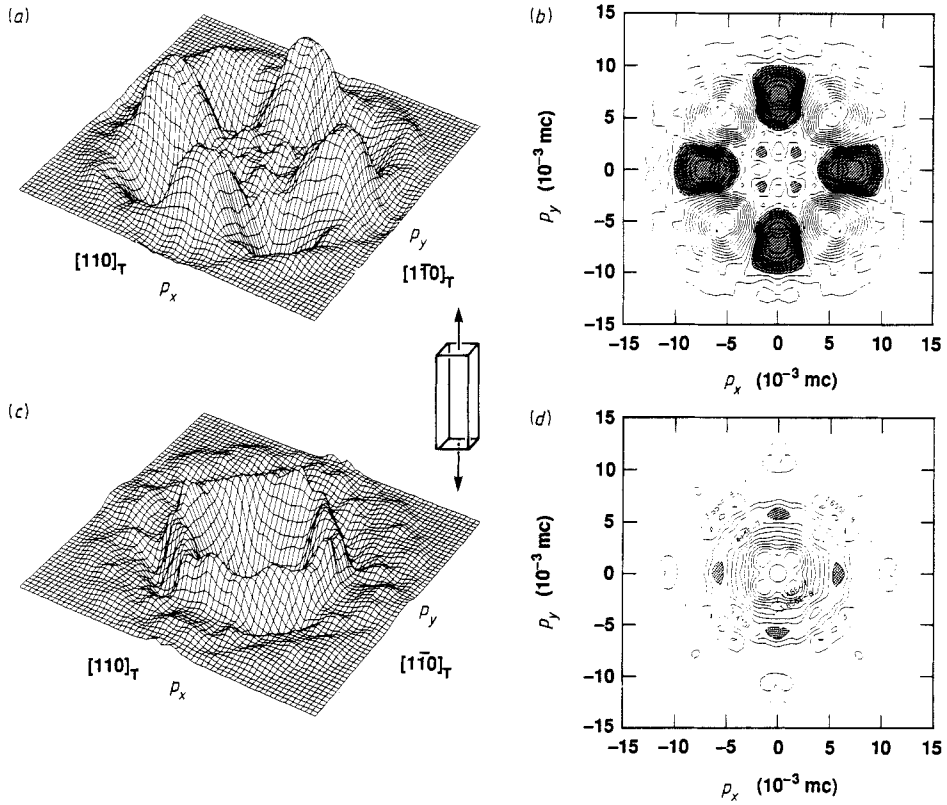

Figure 6. Residual anisotropy surface (*a*) and its associated isodensity contour plot (*b*) for La_2CuO_4 with a [001] integration axis, at $T = 9$ K. The difference between the 298 K and 9 K ACPAR results is illustrated in a 3D representation (*c*) and an isodensity contour plot (*d*). Contour zone above the average has been highlighted.

geometry and a sample temperature of 9 K. In comparing this result with its room-temperature (298 K) counterpart, the surface of figure 5(*a*), we see slight differences in the peak shapes at higher momenta. Near the centre we also see four distinct small peaks in the 9 K data which are not well resolved at 298 K. A comparison of the 9 K residual anisotropy surface iso-density plot (see figure 6(*b*)) with its 298 K counterpart also reveals small shifts in peak and valley positions. The difference between the 298 K and 9 K ACPAR results is most clearly illustrated in figure 6(*c*). Here the full electron–positron momentum distribution for 9 K has been subtracted from the full distribution for 298 K (see figure 3), after normalising to the total number of counts. The results are displayed after signal averaging and smoothing using the procedure of figure 5. The difference surface represents $0.5 \pm 0.2\%$ of the normalised distributions. The surface and its iso-density plot (figure 6(*d*)) show a transfer of counts into the distribution centre at low temperatures. Similar results are seen in different plots for the 70 K measurements (not shown) in the [100] axis integration geometry. We compare the ACPAR results for the [110] axis integration geometry (along a major twinning axis in the basal plane) at 9 K and 298 K in figures 7 and 8. Again one observes slight changes in peak and valley shape position as well as in resolution. The difference surface represents $0.7 \pm 0.2\%$ of the

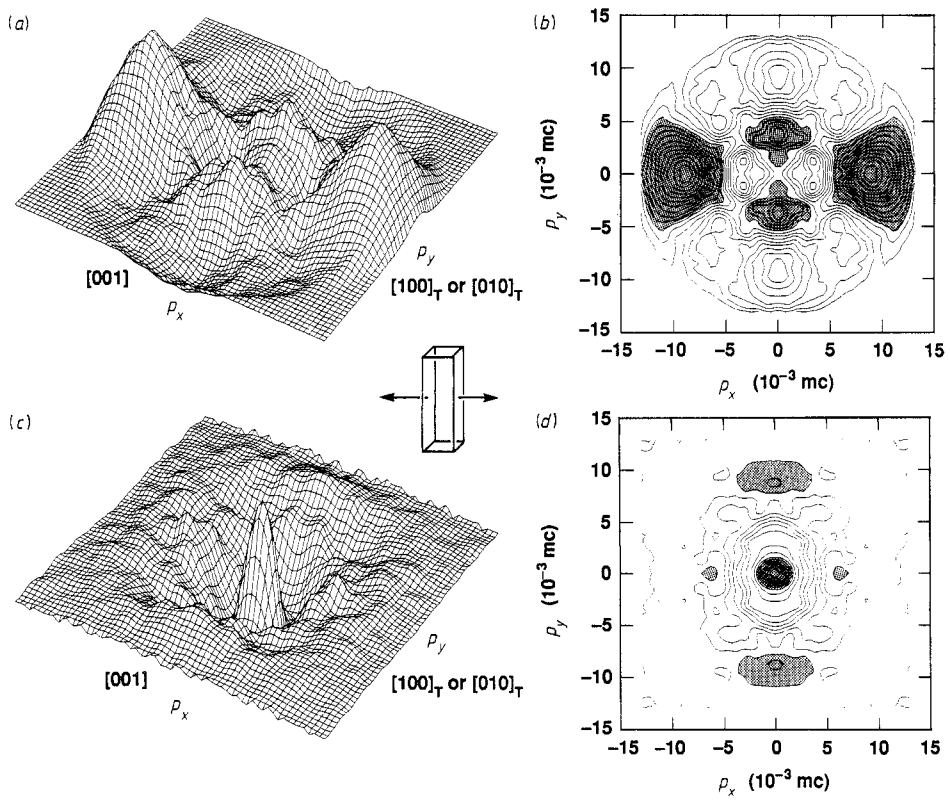

Figure 7. Same as for figure 6, for the [010] integration axis.

normalised distributions. Note the anisotropic shape in the iso-density plot of figure 7(*d*). Figure 8 shows the result of taking the difference between the projections of the 9 K (298 K) data along orthogonal crystalline axes in the right (left) inset.

The temperature effects displayed in figure 6–8 are derived in part from the reduced phonon scattering of the positron probe at low temperatures and the effects of lattice parameter changes. To the extent that the electronic structure of La_2CuO_4 resembles that of NiO [12], these results may reflect changes in the covalency structure, as will be shown in the next section.

Figure 9 shows the result of subtracting from figure 3 a gaussian of revolution containing ~85% of the total counts and fitted to the higher-momentum components of the full distribution of figure 3. The gaussian shape is characteristic of a core electron contribution to the distribution. It is tempting to treat the anisotropic remainder as the manifestation of a Fermi surface [25]. However, the results of such attempts [25] are in substantial disagreement with the predictions of standard band theory. This disagreement motivates an alternative approach which is proposed in the next section.

4. Momentum distribution of the annihilating e^-–e^+ pairs: method of calculation and results

A 2D ACPAR experiment measures a coincidence rate which is proportional to the 2D electron–positron momentum density $\rho^{2\gamma}(p_x, p_y)$, which is in turn related to the full 3D

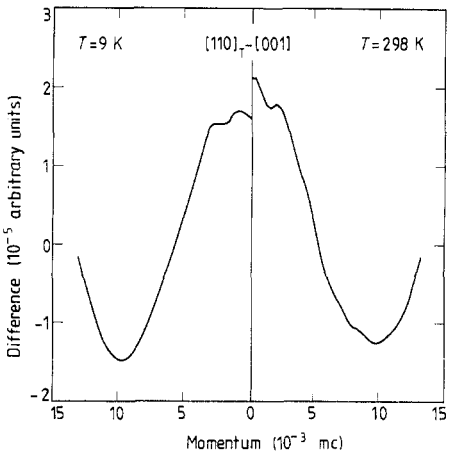

Figure 8. Experimental anisotropy curves, as described in the text, for La_2CuO_4, with integrations along the indicated pair of orthogonal tetragonal axis, at $T = 9$ K (left inset) and 298 K (right inset).

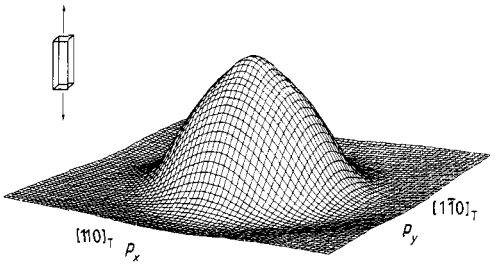

Figure 9. 2D ACPAR spectrum obtained after subtraction from figure 3 of a gaussian of revolution fitted to the higher momentum of the distribution given in figure 3 (momentum integration direction along the c axis).

momentum distribution of annihilating pairs by:†

$$\rho^{2\gamma}(p_x, p_y) = \int_{-\infty}^{+\infty} \mathrm{d}p_z \rho^{2\gamma}(\boldsymbol{p}).$$

In principle, it is the one positron–many electron many-body system for which the momentum density is measured. However, if the deformation effect of the positron on the electron density is neglected,‡ this simply reduces to

$$\rho^{2\gamma}(\boldsymbol{p}) \propto \sum_{j\,\mathrm{occ}} |\chi^j(\boldsymbol{p})|^2$$

where the sum extends over all occupied electronic states, $\chi^j(\boldsymbol{p})$ is the so-called probability amplitude for the emission of two photons with total momentum $\boldsymbol{p} = \hbar\boldsymbol{k}$, resulting from the annihilation of a positron with an electron in a state j whose wavefunction is ψ^j.

$\chi^j(\boldsymbol{p})$ is given by the Fourier transform of the wavefunction product:

$$\chi^j(\boldsymbol{k}) = \int \mathrm{d}^3\boldsymbol{r}\psi^j(\boldsymbol{r})\Psi^+(\boldsymbol{r}) \exp(-\mathrm{i}\boldsymbol{k}\cdot\boldsymbol{r}).$$

† To make a connection with experiment, the convolution of $p^{2\gamma}(p_x', p_y')$ with an instrumental resolution function should be performed:

$$\Gamma^{2\gamma}(p_x, p_y) = \int \mathrm{d}p_x' \cdot \mathrm{d}p_y' \cdot R(p_x' - p_x, p_y' - p_y) \cdot \rho^{2\gamma}(p_x', p_y').$$

In the following the two-dimensional R function is taken to be a gaussian with a standard deviation of 0.2 mrad (0.33 mrad FWHM), while the experimental resolution was actually somewhat greater at 0.5 mrad.

‡ Usually the instantaneous electron density at the positron site is much larger than that assumed in the absence of positron (the positron acting as an attractive centre for the negative cloud), due to correlations between the positron and neighbouring electrons. But in spite of this enhancement factor, the momentum distribution is often fairly close to the one obtained without taking into account these correlations (hypothesis of the so-called independent particle model approximation, IPM).

4.1. LCAO-MO prescription

In the IPM framework, the problem is to calculate ψ^j and Ψ^+. In the previous section a trial function for the positron was proposed. Because the phase of the positron wavefunction is supposed to be constant over at least the closest atomic cells, a 2D ACPAR experiment will be able to sample the phase relations between the electronic states on the neighbouring sites: phase relations which will be preserved in the corresponding state of the annihilating e^-–e^+ pairs. Therefore we have possible access to the covalency structure of the material.

Excluding core electrons which are assumed to give a gaussian contribution to the angular correlation curves, it is still necessary to have an adequate description of the valence electrons. At present, there are two limiting theories for the outer electrons in a solid: crystal field theory and band theory. The former rests on the assumption that the interactions between neighbouring atoms are so weak that each electron remains localised at a discrete atomic position. On the other hand, band theory assumes that the interaction between neighbouring atoms is so large that each electron is shared equally by all like nuclei. This approach fails to treat adequately the electron–electron correlations, which are of increasing importance as the interactions between the neighbouring atoms become weaker.

This failure is clearly apparent when photoemission spectroscopy measurements (XPS, UPS, inverse photoemission) [6] performed on these perovskite oxides are compared with standard band theory calculations [5]. In these oxides the intermediate character of the d type of outer electrons, which seems actually to exhibit a more subtle balance between localised and itinerant electronic characters, is primarily responsible for this failure. The apparent lack of Fermi surface in the angular correlation curves of 2D ACPAR and the well defined features of the residual anisotropy contour maps in La_2CuO_4 (see figure 5) tend to confirm this speculation. From this argument, a method based on a LCAO-MO picture in the limit of the localised ion scheme will be developed in order to calculate the electronic structure of these perovskite oxides. The localised ion scheme leads to a local description of the perovskite in terms of small clusters: here the metal (copper) surrounded by its nearest oxygen neighbours (ligands).

This scheme is doubly justified in the present context: (i) a fairly localised electronic character; and (ii) a free volume for the positron, as shown in § 2, concentrated around the copper–oxygen bonds. This prescription is based on earlier successful studies which accounted for the main features encountered in PAS investigation of various oxides such as NiO [12], Fe_3O_4 [13, 20] and $Na_{0.64}WO_3$ [23]. Thus the jth state of a valence electron will be written as a linear combination of atomic orbitals centred around the sites i of the cluster so considered:

$$\psi^j(\boldsymbol{r}) = \sum_i c_{ij}\varphi_i^j(\boldsymbol{r}_i)$$

where $\boldsymbol{r}_i = \boldsymbol{r} - \boldsymbol{R}_i$ and φ_i^j is given by the usual expression

$$\varphi_i^j(\boldsymbol{r}_i) = R_{nl}(r_i)Y_{lm}(\Theta_i, \Phi_i)$$

(here the index j refers to the set of quantum numbers n, l and m). The probability amplitude $\chi^j(\boldsymbol{k})$ for the emission of 2γ with total momentum $\boldsymbol{p} = \hbar\boldsymbol{k}$ is given by

$$\chi^j(\boldsymbol{k}) = \sum_i c_{ij} \int \mathrm{d}^3\boldsymbol{r}\varphi_i^j(\boldsymbol{r} - \boldsymbol{R}_i)\Psi^+(\boldsymbol{r}) \exp(-\mathrm{i}\boldsymbol{k}\cdot\boldsymbol{r}).$$

By expanding the $\exp(\mathrm{i}\boldsymbol{k}\cdot\boldsymbol{r})$ in terms of spherical harmonics, $\chi^j(\boldsymbol{k})$ takes the form

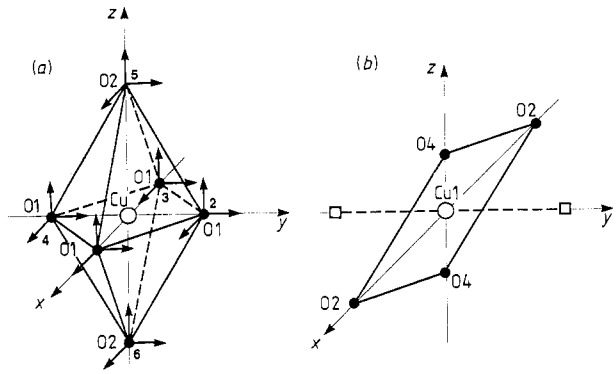

Figure 10. Coordinate system for the cluster of oxygens around a copper site, representative of La_2CuO_4 (*a*) and $YBa_2Cu_3O_7$ (*b*).

$$\chi^j(\boldsymbol{k}) = (4\pi)^2 \sum_i c_{ij} \exp(-\mathrm{i}\boldsymbol{k}\cdot\boldsymbol{R}_i)(-i)^l Y^*_{lm}(\Theta_k, \Phi_k) K_{nl}(k)$$

where $K_{nl}(k)$ represents the radial part of the atomic momentum wavefunction:

$$K_{nl}(k) = \int_0^\infty r_i^2 \, \mathrm{d}r_i R_{nl}(r_i)\Psi^+(r_i) j_l(kr_i)$$

and $j_l(kr_i)$ is the spherical Bessel function of order l. As the positron wavefunction is spherically symmetric around each ion core, the angular dependence of the wavefunction product is the same as that for the electrons.

Because there is a need to preserve the simplicity of the approach, we will only consider in the following the last occupied valence states, mainly the antibonding states which are formed between the 3d states of copper and the 2s and 2p states of the surrounding oxygens (4 O1 and 2 O2 in the case of La_2CuO_4 and 2 O1 and 2 O4 in the case of $YBa_2Cu_3O_7$). The clusters so defined [18] are given in figure 10. Therefore the ψ^j will be the resulting crystal field-localised orbitals of appropriate symmetry [29].

In order to take proper account of the Jahn–Teller type of distortion of the cluster, the covalency parameters (in fact the covalency overlap parameters, because they are defined for the antibonding states) c_ν^α ($\nu = \sigma, \pi, \mathrm{s}$) will be given separate values for different directions: $\alpha = b$ basal plane or x–y directions and c along the c axis or z direction [29]. The antibonding MO combinations for La_2CuO_4 are written as [29]:

$$t_{2g}\text{ states: } \psi^{xy}(r) = N_{xy}[\mathrm{d}_{xy} - c_\pi^b(\mathrm{p}_1^y + \mathrm{p}_2^x - \mathrm{p}_3^y - \mathrm{p}_4^x)/2]$$

$$\psi^{yz}(r) = N_{yz}[\mathrm{d}_{yz} - c_\pi^b(\mathrm{p}_2^z - \mathrm{p}_4^z)/\sqrt{2} - c_\pi^c(\mathrm{p}_5^y - \mathrm{p}_6^y)/\sqrt{2}]$$

$$\psi^{zx}(r) = N_{zx}[\mathrm{d}_{zx} - c_\pi^b(\mathrm{p}_1^z - \mathrm{p}_3^z)/\sqrt{2} - c_\pi^c(\mathrm{p}_5^x - \mathrm{p}_6^z)/\sqrt{2}]$$

$$e_g\text{ states: } \psi^{z^2}(r) = N_{z^2}[\mathrm{d}_{z^2} - c_\sigma^b(\mathrm{p}_1^x + \mathrm{p}_2^y - \mathrm{p}_3^x - \mathrm{p}_4^y)/2$$

$$-c_\sigma^c(-\mathrm{p}_5^z + \mathrm{p}_6^z)/\sqrt{2} + c_\mathrm{s}^b(\mathrm{s}_1 + \mathrm{s}_2 + \mathrm{s}_3 + \mathrm{s}_4)/2 - c_\mathrm{s}^c(2\mathrm{s}_5 + 2\mathrm{s}_6)/\sqrt{2}]$$

$$\psi^{x^2-y^2}(r) = N_{x^2-y^2}[\mathrm{d}_{x^2-y^2} - c_\sigma^b(-\mathrm{p}_1^x + \mathrm{p}_2^y + \mathrm{p}_3^x - \mathrm{p}_4^y)/2$$

$$-c_\mathrm{s}^b(\mathrm{s}_1 - \mathrm{s}_2 + \mathrm{s}_3 - \mathrm{s}_4)/2].$$

The numbers 1, 2 . . . 6 refer to ligands along the principal axis of the octahedron as reported in figure 10 and the N are the normalisation constants of the open-shell MO.

The momentum wavefunctions of electron–positron pairs associated with these five states are obtained by making use of the expression for $\chi^j(\boldsymbol{p})$. Then the momentum density $\rho^{2\gamma}(\boldsymbol{p})$ is calculated by summing over this restricted set of occupied states. In the particular case of La_2CuO_4, due to the ligand field, the d levels of the metal split into a threefold t_{2g} level and a twofold e_g level. In addition to this splitting, the elongation of the octahedron along the c axis will induce additional splitting of the t_{2g} in d_{xz}, d_{yz} and d_{xy}, and of the e_g in d_{z^2} and $d_{x^2-y^2}$.

Finally, following the arguments developed by Goodenough [30–34], the $x^2 - y^2$, σ^* in character, will be split by an intra-coulombic interaction. Therefore a d^9 configuration for copper leads to the following expression for $\rho^{2\gamma}(\boldsymbol{p})$:

$$\rho^{2\gamma}(\boldsymbol{p}) = 2\{|\chi^{xy}(\boldsymbol{p})|^2 + |\chi^{yz}(\boldsymbol{p})|^2 + |\chi^{zx}(\boldsymbol{p})|^2\} + |\chi^{x^2-y^2}(\boldsymbol{p})|^2 + 2|\chi^{z^2}(\boldsymbol{p})|^2.$$

An integration along a particular momentum direction of $\rho^{2\gamma}(\boldsymbol{p})$ followed by the convolution with an instrumental resolution function [28] leads to the quantity $\Gamma^{2\gamma}(p_x, p_y)$, which can be compared with the experimental results.

4.2. *LCAO–MO results*

When applied to La_2CuO_4, the momentum wavefunctions $\chi^j(\boldsymbol{p})$ are calculated with the atomic wavefunctions of Cu^{2+} in a d^9 configuration resulting from a Herman and Skillman scheme [14] and the atomic wavefunctions 2s and 2p of O^{2-} (in a +1 well) given by Watson [35].

The six covalency-overlap parameters c_ν^α ($\nu = \sigma, \pi, \delta$ and $\alpha = b, c$) were determined by a non-linear least-squares fitting procedure in order to attain the best resemblance with the 2D ACPAR residual anisotropy distribution results of La_2CuO_4 for a momentum integration along the [010] direction (see figure 5(*b*)). The covalency-overlap parameters thus obtained take the values

$$c_\sigma^b = 0.1500 \qquad c_\pi^b = 0.0120 \qquad c_s^b = 0.00300$$

$$c_\sigma^c = 0.0375 \qquad c_\pi^c = 0.0030 \qquad c_s^c = 0.00075.$$

Incidently, the expected hierarchy applies to our results, i.e.

$$c_\sigma \gg c_\pi \gg c_s > 0$$

$$c^b \gg c^c > 0$$

which indicates a stronger orbital overlap in the basal plane than along the c axis.

Calculations of residual anisotropies using these parameters have been performed, following the same procedure applied to the experimental data (see § 3). Surface and iso-density contour plots of the calculated anisotropies, in the three sample geometries, are shown in figure 11. The theoretical results compare favorably with their experimental counterparts given in figure 5.

It is also interesting to display for further checks the anisotropy curves resulting from the difference of the 2D momentum distribution integrations along the orthogonal axis:

$$A(p) = \int \mathrm{d}p_y\, \Gamma^{2\gamma}(p, p_y) - \int \mathrm{d}p_x\, \Gamma^{2\gamma}(p_x, p).$$

The comparison between theory and experiment is given in figure 12. Qualitative agreement is achieved, but discrepancies in peak locations and additional experimental

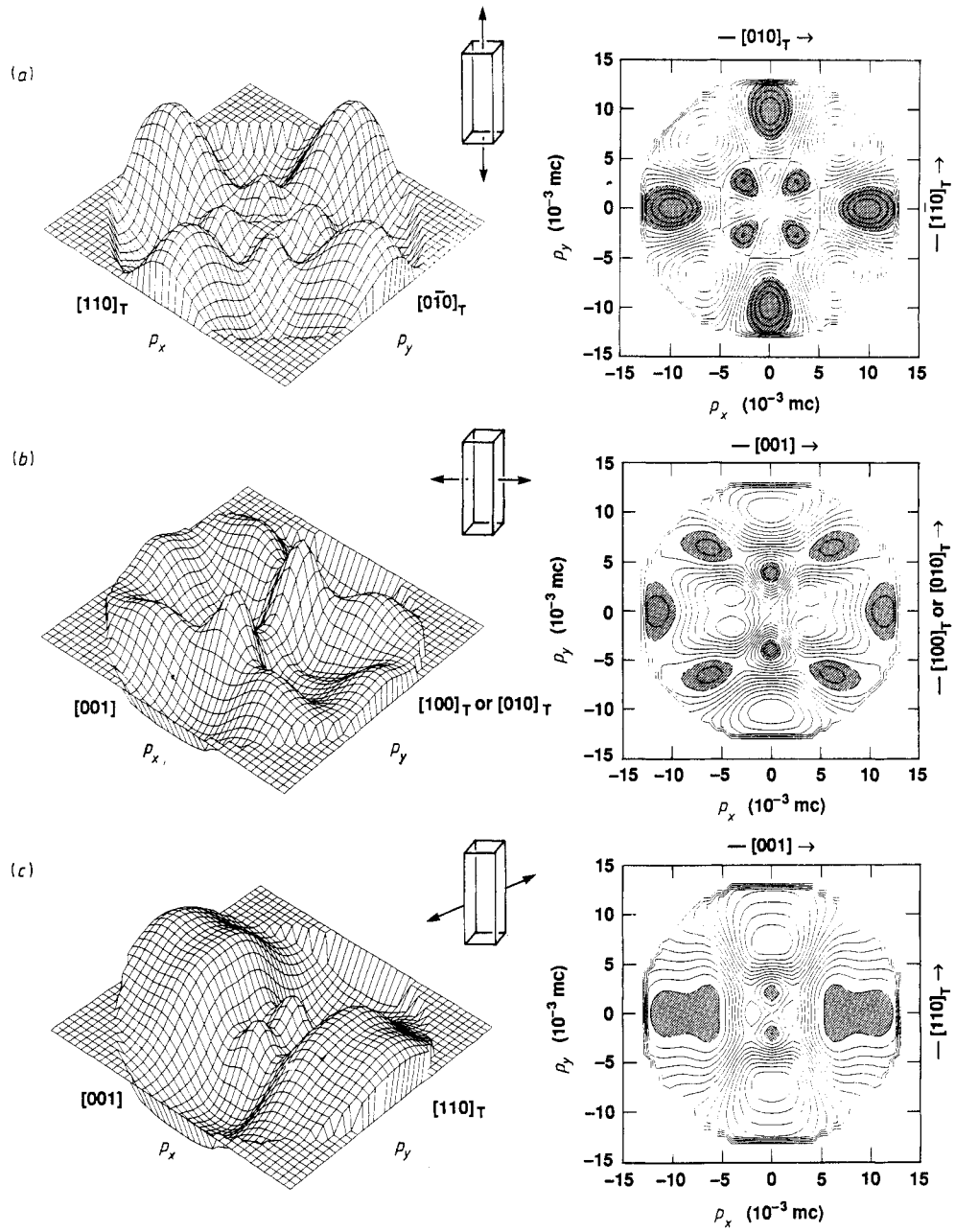

Figure 11. Theoretical counterparts of figure 5.

residual features not present in the calculated LCAO–MO model are evident, which most likely arise from the extreme simplicity of the model itself.

However, given the surprising success of this approach, it is now worth studying the decomposition of the residual anisotropy distributions in their various contributions in order to analyse the features in terms of covalency effects. The two peak features

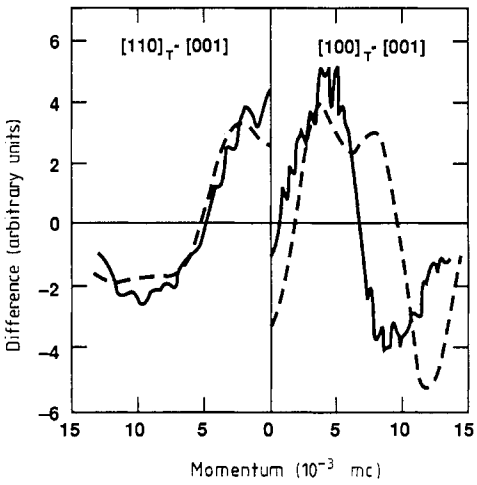

Figure 12. Experimental (theoretical) anisotropy curves $A(p)$, as described in the text, for La_2CuO_4, with integrations along the indicated pairs of orthogonal crystalline axis. Experimental (theoretical) curves for each inset are denoted by full (broken) curves.

occurring at low momentum in figures 11(*b*) and (*c*) (see also figures 5(*b*) and (*c*)) can be attributed essentially to the e_g contribution. More precisely, in the case of figure 5(*b*) (or 11(*b*)) the mixing of the Cu-$3d_{z^2}$ and oxygen-$2p_z$ is involved (see figure 13(*a*)), whereas in the case of figure 5(*c*) (or 11(*c*)) the mixing of Cu-$3d_{x^2-y^2}$ and oxygen-$2p_x$ and $2p_y$ gives most of the contribution (see figure 13(*b*)). In the same way, when the momentum integration is along the *c* axis, the four peaks located along the orthorhombic axis in momentum space are explained by a major t_{2g} contribution. For this sample orientation, at low momentum, the delicate balance among the overlap occurring between oxygen-2p and 2s and Cu-$3d_{x^2-y^2}$ (along the orthorhombic axis) and Cu-$3d_{z^2}$ (along the tetragonal axis) is reflected in the experimental temperature variations of the residual anisotropy distributions (see figures 6–9 and figure 13(*c*)).

In the three cases, the extra features which occur essentially at high momenta are the result of the interference terms due to the mixing of 3d and 2s and 2p when evaluating the $|\chi^j(\boldsymbol{p})|^2$.

4.3. Consequences of LCAO-MO *description*

From this study, based upon the LCAO-MO description, a few major consequences are expected.

(i) A reduction of the Cu moment due to covalency effects and its implication on the magnetic form factor for copper, especially at low scattering angle where a forward peak is expected. Such consequences were already noticed in the case of K_2CuF_4 [36] and preliminary neutron scattering experiments performed on La_2CuO_4 [37] seem to confirm such expectation.

(ii) A distortion of the transition probabilities by covalency effects in the valence band spectra as obtained by x-ray photoemission spectroscopy. This point is well documented for other oxides such as ReO_3 [38]. Within this simple approach, such detailed experiments must lead to a better knowledge of the covalency structure in these oxides, in particular information on the metal to ligand spin transfer, if one also includes magnetic resonance spectroscopy measurements (nuclear magnetic resonance, electron

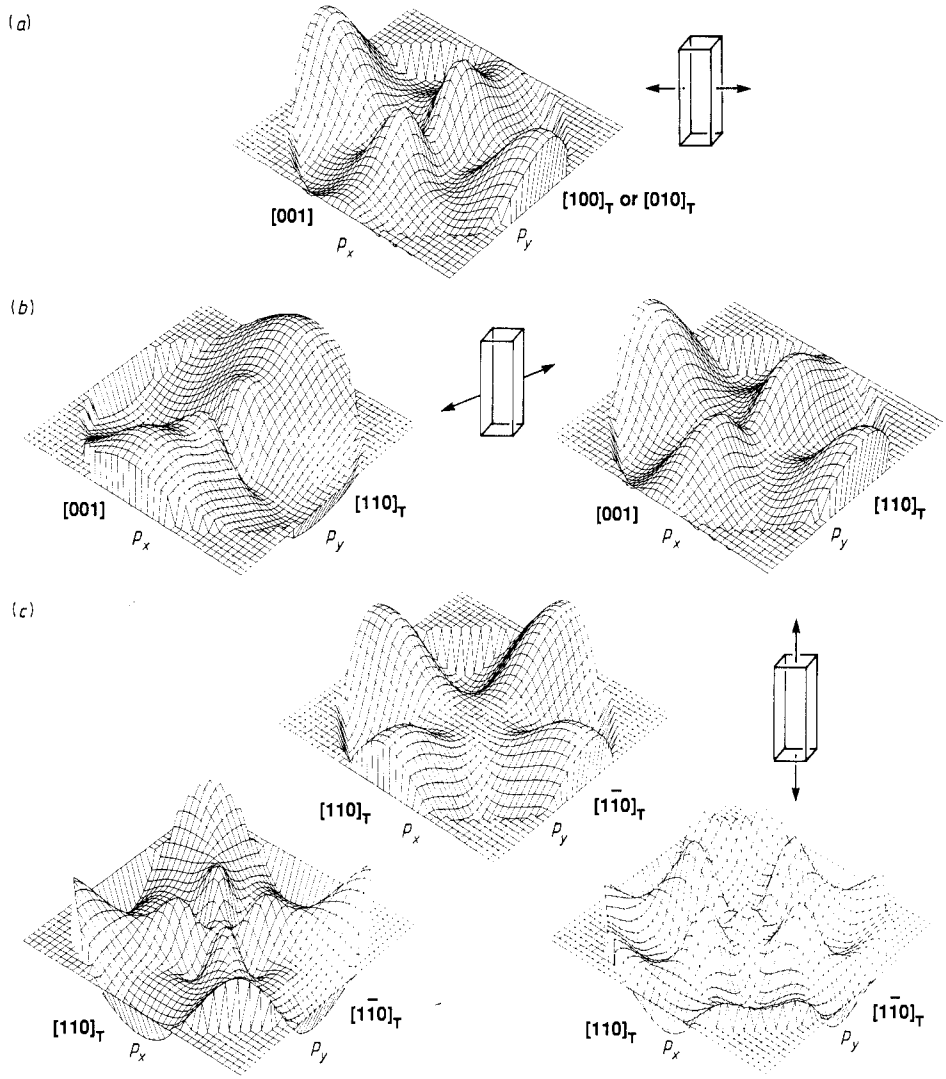

Figure 13. Partial 3D residual anisotropy surfaces in the three samples geometries given in the insets. (*a*) z^2; (*b*) $x^2 - y^2$ (left) and z^2 (right); (*c*) t_{2g}, $x^2 - y^2$ (bottom left) and z^2 (bottom right) contributions to the total 3D residual anisotropy surfaces given in figures 11(*b*), (*c*) and (*a*) respectively.

paramagnetic resonance or electron–nuclear double resonance) which are not yet fully available.

5. Electron momentum density determination: Lock–Crisp–West folding analysis

We saw in the previous section that a crystal-field theory model for the electronic states of La_2CuO_4 gave satisfactory qualitative agreement between theory and experiment.

Here we shall assume another extreme of physical behaviour and invoke a band theoretical picture in an attempt to extract the reciprocal space electron momentum density from our 2D ACPAR data.

It has been known for a long time [39] that the ACPAR technique measures the real momentum distribution of electrons in a crystal (as modulated by the positron momentum distribution) and not the electronic distribution in $\boldsymbol{k}$ space. Thus one can interpret 2D angular correlation results in a metal as arising from:

(i) states in full Brillouin zones which contribute a continuous distribution having the point symmetry of the reciprocal lattice;

(ii) contributions from a partially filled zone which are non-vanishing only at a momentum $\boldsymbol{p}$ such that $\boldsymbol{p}$–$\boldsymbol{G}$ lies inside the Fermi surface;

(iii) contributions of an additional, often large, isotropic 'core' contribution from annihilation of electrons in several full Brillouin zones [40].

Assumptions must be made about the shape of the contributions due to 'core-like' electrons in filled shells; these contributions may appear in several full Brillouin zones.

In practice, various effects complicate the interpretation scheme above. The positronic wavefunction overlaps with states of different angular momenta may not be identical [41]. The positron polarises the electronic medium of the solid. Electron–electron correlations may differently affect the momentum state densities of the filled and partially filled bands. And there is frequently uncertainty about the precise nature of the broad 'core' contribution.

Nevertheless, it is possible to extract the Fermi surface topology for metals from 2D ACPAR data with reasonable accuracy. Lock *et al* [40], Lock and West [42] and Beardsley *et al* [43] have developed a superposition procedure (subsequently referred to as LCW) whereby the measured electron–positron momentum density is transformed into a Bloch wavevector $\boldsymbol{k}$ space electron–positron momentum density $\rho^{2\gamma}(\boldsymbol{k})$. In this function, the singularities and other features that reflect the Fermi surface are isolated and emphasised; the perturbations caused by positron wavefunction and electronic correlation effects usually appear as a smaller (relative to their effect on $\rho^{2\gamma}(\boldsymbol{p})$) perturbation of $\rho^{2\gamma}(\boldsymbol{k})$ from the equivalent electron $\boldsymbol{k}$ space density $\rho_e(\boldsymbol{k})$.

The power of this technique to establish the essential topology of a complex Fermi surface of several sheets, through simple and easily readable contour displays, has now been established in several works [41, 44].

We have applied the LCW formalism to our La_2CuO_4 data. Figure 14 shows an isodensity contour plot of the two-dimensional $\rho^{2\gamma}(\boldsymbol{k})$. The integration axis is [001], and the Brillouin zone of the twinned, face-centred orthorhombic crystal has been referred to the body centred tetragonal lattice, with $a = 3.8011$ Å and $c = 13.149$ Å. The minimum value is 98% of the maximum. LCW computations for other integrations of the La_2CuO_4 two-photon momentum distributions (not shown) give qualitatively similar results for their extremal variations.

The original full 2D ACPAR distribution (not shown) from which this approximate electron momentum density (EMD) was derived was a square 128×128 2D histogram centred about the origin with a bin width of 0.416×10^{-3} mc. It contained about 25 million counts and $\sim 10^4$ counts in the peak channel. The 2D EMD of figure 14 contains an average of $\sim 6 \times 10^4$ counts per bin, giving a corresponding statistical noise limit of the order of 0.1%. Thus the residual differences shown in figure 14 are statistically significant and their existence requires additional explanation.

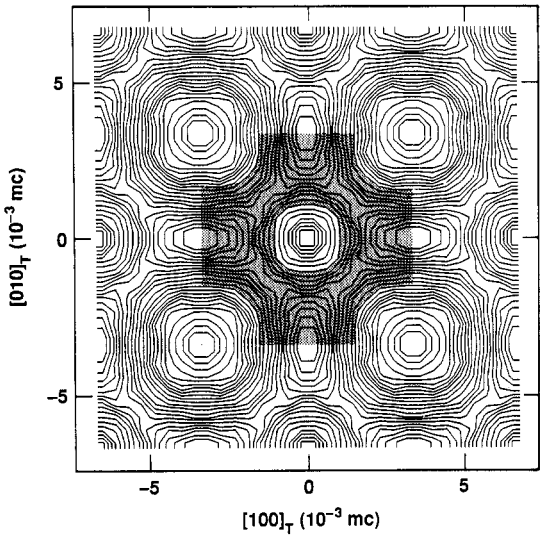

Figure 14. Isodensity contour plot of a LCW folded spectrum in a repeated-zone scheme for La_2CuO_4. The integration axis is along [001]. The crystalline axes have been referred to the body-centred tetragonal lattice. Maximum to minimum variation is 2% and values below the average have been highlighted.

It is unlikely that the residual differences are derived from a Fermi surface. The 2D EMD is nearly constant, a result close to that expected from filled bands [40, 43]. Small residual variations of this order (~2%) have been observed in the LCW analysis of 1D ACPAR data for the semiconductor (narrow band gap insulator) germanium [42]. Thus, it is more likely that the residual variation originates from the positronic wavefunction differently overlapping different electronic states [41], and/or from electron–electron correlation effects. Further investigations of the positronic wavefunction in La_2CuO_4 would be useful to clarify this point.

The assumption of filled-band behaviour can be tested by observing the magnitude of the oscillatory residual structure. If the EMD is governed by LCW of filled bands, the oscillation amplitude should have a minimum when the 2D data is superposed upon itself with shift displacements equal to the reciprocal lattice vectors of the projected 2D Brillouin zone. A similar result holds for the residual behaviour of the LCW results from 1D ACPAR measurements [43]. In figure 15 we plot the quantity

$$[\rho^{2\gamma}_{\max}(k_x, k_y) - \rho^{2\gamma}_{\min}(k_x, k_y)]/\rho^{2\gamma}_{\max}(k_x, k_y)$$

as a function of the shift distance G^*_{100} for the data of figure 14. The residual oscillations are represented by a broken curve. The vertical broken line locates the reciprocal lattice wavevector a^*_0 derived from the lattice constants of the BCT cell to which the data are referred. There is a clear minimum in the vicinity of the physical shift distance, a result consistent with approximately filled-band behaviour. Other oscillatory minima occur at integral half-multiples of the physical G^*_{100}. For comparison, we have also plotted (full curve) the normalised oscillatory amplitude for a gaussian of revolution fit to the high-momentum components of the parent distribution and superposed with the same shift distances. As expected, the amplitude monotonically increases as a function of G^*_{100}.

6. Discussion and summary

Because the details of the theoretical predictions depend closely upon the covalency overlap parameters of the Cu–O valence bonding, the experimental features which show

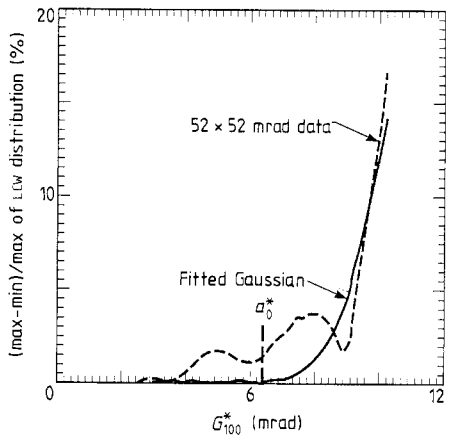

Figure 15. Residual behaviour of the LCW spectrum of figure 14 as a function of the shift distance G_{100}^*, as indicated by the broken curve. The full curve indicates the normalised oscillatory amplitude for a gaussian of revolution fit to the high-momentum components of the parent distribution.

up in the residual anisotropy distributions are expected to be sensitive to the presence of a dopant, like Sr in the case of La_2CuO_4, as well as to the temperature when crossing T_c. In the present context the dopant will act at two different levels: (i) by changing the positron free volume due to the substitution of Sr for La, which modifies the bond distances and the atomic volume; (ii) by modifying the covalency overlap parameters associated with the resulting charge redistribution on the copper site, in accordance with first-principles calculations [45].

If we consider a random distribution of Sr on the La sites and the crystallographic data relative to $La_{1.85}Sr_{0.15}CuO_4$ [46], the positron wavefunction, as calculated in § 2, is described with the α parameters given in table 1. With respect to the results for pure La_2CuO_4, the higher value of α_{Sr} compared with α_{La} leads to a greater extension of the positron wavefunction outside the basal plane. This positron effect, in conjunction with a change in the covalency structure of the doped materials, are expected to change noticeably the 2D ACPAR results, as the preliminary results of reference [47] seem to prove.

Although the calculations have been centred on La_2CuO_4, a similar approach may be applied to $YBa_2Cu_3O_7$. As stated in § 4.1, one can start with the minimum cluster defined by the square planar distribution of oxygens (O1 and O4) around the copper Cu1, where most of the annihilation is assumed to take place (see § 2). By combining the positron wavefunction described in § 2 with the appropriate combinations of atomic orbitals associated with the cluster of figure 10(*b*), one can calculate the momentum density for a d^8 configuration of copper. In figure 16(*a*), we show the resulting residual anisotropy distribution for a momentum direction of integration along the *c* axis. In figure 16(*b*), the residual anisotropy of figure 16(*a*) was added up to its 90° rotated counterpart in order to take into account the twining inherent to $YBa_2Cu_3O_7$. The calculations compare favorably with the experimental result of reference [28]. Further details will be given in a forthcoming paper.

On the basis of this simplified theoretical model, it was shown that the experimental anisotropy distributions can be qualitatively described in terms of the particular covalency structure used here to describe the outermost valence electrons in La_2CuO_4. Besides this overall agreement, the remaining discrepancies can be attributed to: (i) electronic transfer between nearest-neighbour copper atoms and partial oxygen–oxygen

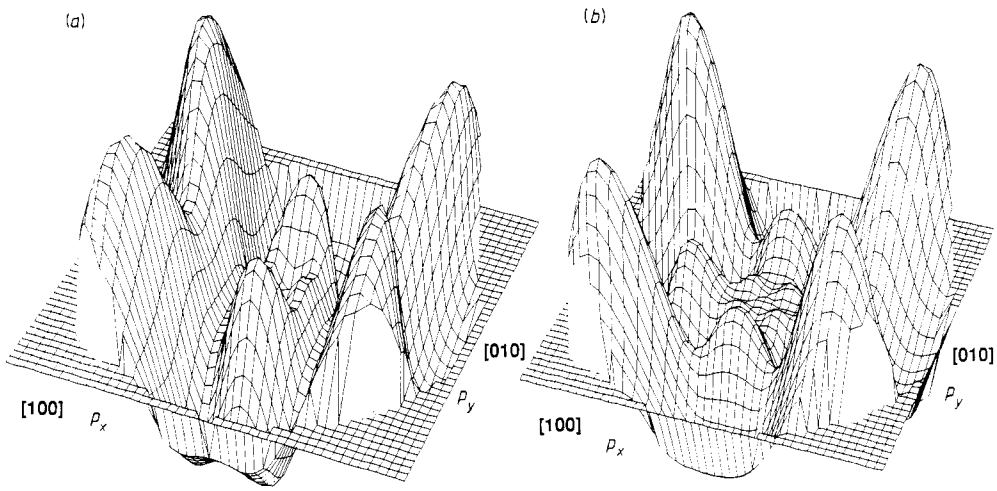

Figure 16. 3D residual anisotropy surface of the electron–positron annihilation momentum distribution of $YBa_2Cu_3O_7$ with a momentum direction of integration along the c axis (a). The result corrected for twinning is displayed in (b). The values of p_x and p_y, along the [100] and [010] directions, range between -15 and $+15 \times 10^{-3}$ mc.

overlap; (ii) a more rapid decrease in the radial component of the momentum wavefunction, the K_{nl}, than found in our model; (iii) spatial anisotropic features in the positron wavefunction which can be important in the present case of highly anisotropy crystalline structure when dealing with such small residual anisotropies in the momentum density; and (iv) positron–electron correlation effects affecting differently the excitation of the MO states induced by the screened positron coulombic field. The first three points can be taken care of by performing more sophisticated calculations on realistic molecular clusters representative of the actual perovskite oxide. In this spirit, the multiple scattering $X\alpha$ cluster method or the configuration interaction approach would be highly desirable. The last point is more difficult to account for, at the present stage, although a certain number of attempts have been suggested recently [48] to go beyond the IPM approximation.

To summarise, it was shown that PAS is a useful technique for studying high-T_c materials. It is fortunate that, in the nearly defect-free version of the so-called 214 and 123 perovskite oxides, the Bloch state of the positron is probing the Cu–O bonding: this part of the material which is supposed to give the high-T_c properties that we know. We also explain the residual anisotropies obtained from 2D ACPAR measurements on La_2CuO_4 within a LCAO–MO scheme in its simplest version, implying a fairly localised electronic character. Specifically, a highly anisotropic covalency structure was found which would describe the annihilation of the last occupied valence electronic states with the positron wavefunction with a delicate balance between Cu-$3d_{x^2-y^2}$ and $3d_{z^2}$ states, as is revealed in the temperature effects on the 2D ACPAR spectra. On the other hand, the application of the LCW folding analysis to La_2CuO_4 yields a result very close to filled-band behaviour. We believe the deviations from this insulator situation are significant, but that they primarily originate from positronic wavefunction mixing of the electronic states and not from a Fermi surface effect. The similarities encountered between the LCW results for La_2CuO_4 and NiO [49] suggest that one should be careful in the application of

the LCW theorem and the interpretation of the resulting EMD. In the doped material $La_{2-x}Sr_xCuO_4$ and in $YBa_2Cu_3O_7$, positron wavefunction effects are expected to dominate although Fermi surface features, weak in magnitude due to the small number of electrons at the Fermi energy, must show up experimentally at higher statistics.

Acknowledgments

This work was performed under the auspices of the US Department of Energy by the Lawrence Livermore National Laboratory under the contract number W-7405-ENG-48. J H Kaiser would like to thank the Robert A Welch Foundation (grant No Y-1135) for partial support for this work.

References

[1] Muller-Buschbaum H 1977 *Angew. Chem. Int. Ed. Engl.* **16** 674
[2] Michel C and Raveau B 1984 *Rev. Chim. Min.* **24** 407
[3] Bednorz J G and Müller K A 1986 *Z. Phys.* B **64** 189
[4] Wu M K, Ahburn J R, Torng C J, Hor P M, Meng R L, Gao L, Huang Z J, Wang Y Q and Chu C W 1987 *Phys. Rev. Lett.* **58** 908
[5] Mattheiss L F 1987 *Phys. Rev. Lett.* **58** 1028
Yu J, Freeman A J and Xu J H 1987 *Phys. Rev. Lett.* **58** 1035
Pickett W E, Krakauer H, Papaconstantopoulos D A and Boyer L L 1987 *Phys. Rev.* B **35** 7252
Oguchi T 1987 *Jap. J. Appl. Phys.* **26** L417
Fujiwara T and Hatsugai Y 1987 *Jap. J. Appl. Phys.* **26** L716
Mattheiss L F and Hamann D R 1987 *Solid State Commun.* **63** 395
Ching W Y, Xu Y, Zhao G L, Wong K W and Zandiehnadem F 1987 *Phys. Rev. Lett.* **59** 1333
Temmerman W, Szotek Z, Durham P J, Stocks G M and Sterne P A 1987 *J. Phys. F: Met. Phys.* **17** L319
Herman F, Kasowski R V and Hsu W Y 1987 *Phys. Rev.* B **36** 6904
Bullett D W and Dawson W G 1987 *J. Phys. C: Solid State Phys.* **20** L853
Massida S, Yu J, Freeman A J and Koelling D D 1987 *Phys. Lett.* **A122** 198
Yu J, Massida S, Freeman A J and Koelling D D 1987 *Phys. Lett.* A **122** 203
[6] Fujimori A, Takayama-Muromachi E, Uchida Y and Okai B 1987 *Phys. Rev.* B **35** 8814
Fujimori A, Takayama-Muromachi E and Uchida Y 1987 *Solid State Commun.* **63** 857
Steiner P, Courths R, Kinsinger V, Sander I, Siegwart B, Hufner S and Politis C 1987 *Appl. Phys.* **A44** 75
Reihl B, Riesterer T, Bednorz J G and Müller K A 1987 *Phys. Rev.* B **35** 8804
Iqbal Z, Leone E, Chin R, Signorelli A J, Bose A and Eckhardt H 1987 *J. Mater. Res.* **2** 768
Brown F C, Chiang T C, Friedmann T A, Ginsberg D M, Kwawer G N and Miller T 1987 *J. Low Temp. Phys.* **69** 151
Nucker N, Fink J, Renker B, Ewert D, Politis C, Weiss P J W and Fuggle J C 1987 *Z. Phys.* B **67** 9
Yarmoff J A, Clarke D R, Drube W, Karlsson U O, Taleb-Ibrahimi A and Himpsel F J 1987 *Phys. Rev.* B **36** 3967
[7] Jean Y C, Kyle J, Nakinishi H, Turchi P E A, Howell R H, Wachs A L, Fluss M J, Meng R L, Hor H P, Huang J Z and Chu C W 1988 *Phys. Rev. Lett.* **60** 1069
Jean Y C, Wang S J, Nakanishi H, Hardy W N, Hayden M E, Kiefl R F, Meng R L, Hor H P, Huang J Z and Chu C W 1987 *Phys. Rev.* B **36** 3994
Harshman D R, Schneemeyer J V, Waszczak J V, Jean Y C, Fluss M J, Howell R H and Wachs A L 1988 *Phys. Rev.* B **38** 848
[8] Smedskjaer L C, Veal B W, Legini D G, Paulikas A P and Nowicki L J 1988 *Phys. Rev.* B **37** 2330
Wang S J, Naidu S V, Sharma S C, De D K, Jeong D Y, Black T D, Krichene S, Reynolds J R and Owens J M 1988 *Phys. Rev.* B **37** 603
Usmar S G, Sferlazzo P, Lynn K G and Moodenbaugh A R 1987 *Phys. Rev.* B **36** 8854
Ishibashi S, Yamaguchi A, Suzuki Y, Doyama M, Kumakura H and Togano K 1987 *Jap. J. Appl. Phys.* **26** L688

[9] Berko S 1983 *Positron Solid State Physics* ed W Brandt and A Dupasquier (Amsterdam: North-Holland)
Mijnarends P E 1979 *Positrons in Solids: Topics in current physics No. 12* ed P Hautojarvi (Berlin: Springer)
[10] Mijnarends P E 1987 *Phys. Status Solidi* a **102** 31
[11] Wachs A L, Turchi P E A, Jean Y C, Wetzler K H, Howell R H, Fluss M J, Harshman D R, Remeika J P, Cooper A S and Fleming R M 1988 *Phys. Rev.* B **38** 913
Turchi P E A, Wachs A L, Jean Y C, Howell R H, Wetzler K H and Fluss M J 1988 *Physica* **C153–5** 157
Wachs A L, Turchi P E A, Jean Y C, Wetzler K H, Howell R H, Fluss M J, Harshman D R, Remeika J P, Cooper A S and Fleming R M 1988 *Extended Abstracts: High-Temperature Superconductivity II* (Pittsburgh, Pa.: Materials Research Society) pp 237–40
[12] Chiba T and Tsuda N 1974 *Appl. Phys.* **5** 37
[13] Chiba T 1976 *J. Chem. Phys.* **64** 1182
[14] Herman F and Skillman S 1983 *Atomic Structure Calculations* (Englewood Cliffs, NJ: Prentice-Hall)
[15] Citrin P H and Thomas T D 1972 *J. Chem. Phys.* **57** 4446
Mattheiss L F 1972 *Phys. Rev.* **B5** 290
[16] Longo J M and Raccah P M 1973 *J. Solid State Commun.* **6** 529
[17] Capponi J J, Chaillout C, Hewat A W, Lejay P, Marezio M, Nguyen N, Raveau B, Soubeyroux J L, Tholence J L and Tournier R 1987 *Europhys. Lett.* **3** 1301
[18] von Stetten E C, Berko S, Li X S, Lee R R, Brynestad J, Singh D, Krakauer H, Pickett W E and Cohen R E 1988 *Phys. Rev. Lett.* **60** 2198
[19] Chakraborty B 1982 *Positron Annihilation* ed. P G Coleman, S C Sharma and L M Diana (Amsterdam: North-Holland) 207
[20] Mijnarends P E and Singru R M 1974 *Appl. Phys.* **4** 303
[21] Bleau M, Tsur D, Weger M, Ashkenazi J and Merenda P 1977 *J. Phys. C: Solid State Phys.* **10** 3305
[22] Akahane T, Chiba T and Tsuda N 1979 *J. Phys. Soc. Japan* **46** 815
[23] Akahane T, Hoffmann K R, Chiba T and Berko S 1985 *Solid State Commun.* **54** 823
[24] Kubo Y, Wakoh S and Schwarz K 1981 *J. Phys. Soc. Japan* **55** 1266
[25] Tanigawa S, Mizuhara Y, Hikada Y, Oda M, Suzuki M and Turakami T 1988 *Proc. 1987 MRS Fall Mtg, Boston, MA* **99** 57
[26] Hoffman L, Manuel A A, Peter M, Walker E and Damento M A 1988 *Europhys. Lett.* **6** 61; 1988 *Physica* **C153–5** 129
Peter M, Hoffman L and Manuel A A 1988 *Physica* **C153–5** 1724
Manuel A A 1988 *Helv. Phys. Acta* **61** 451
[27] Smedskjaer L C, Liu J Z, Benedek R, Legnini D G, Lam D J, Stahulak M D, Claus H and Bansil A 1988 *Physica* **C156** 269
Bansil A, Pankaluoto R, Rao R S, Mijnarends P E, Dhugosz W, Prasad R and Smedskjaer L C 1988 *Phys. Rev. Lett.* **61** 2480
[28] Cheong S-W, Fisk Z, Willis J O, Brown S E, Thompson J D, Remeika J P, Cooper A S, Aikin R M, Schiferl D and Gruner G 1990 *Solid State Commun.* in press
[29] Owen J O and Thornley J H M 1966 *Rep. Prog. Phys.* **29** 675
Ballhausen C J and Gray H B 1964 *Molecular Orbital Theory* (New York: Benjamin)
[30] Goodenough J B 1973 *Mater. Res. Bull.* **8** 423
[31] Goodenough J B and Ramasesha S 1982 *Mater. Res. Bull.* **17** 383
[32] Singh K K, Ganguly P and Goodenough J B 1984 *J. Solid State Chem.* **53** 254
[33] Goodenough J B 1988 *Mater. Res. Bull.* **23** 401
[34] Chakraverty B K, Feinberg D, Hang Z and Avignon M 1987 *Solid State Commun.* **64** 1147
[35] Watson R E 1958 *Phys. Rev.* **111** 1108
[36] Hirakawa K and Ikeda H 1974 *Phys. Rev. Lett.* **33** 374
[37] Freltoft T, Shirane G, Mitsuda S, Remeika J P and Cooper A S 1988 *Phys. Rev.* B **37** 137
Vaknin D, Sinha S K, Moncton D E, Johnston D C, Newsam J M, Safinya C R and King H E Jr 1987 *Phys. Rev. Lett.* **58** 2802
[38] Wertheim G K, Mattheiss L F, Campagna M and Pearsall T P 1974 *Phys. Rev. Lett.* **32** 997
[39] West R N 1973 *Adv. Phys.* **22** 263
[40] Lock D G, Crisp V H C and West R N 1973 *J. Phys. F: Met. Phys.* **3** 561
[41] Kaiser J H, Walters P A, Bull C R, Alam A, West R N and Shiotani N 1988 *J. Phys. F: Met. Phys.* **17** 1243
Kaiser J H, West R N and Shiotani N 1986 *J. Phys. F: Met. Phys.* **16** 1307
[42] Lock D G and West R N 1975 *Appl. Phys.* **6** 249

[43] Beardsley G M, Berko S, Mader J J and Shulman M A 1975 *Appl. Phys.* **5** 375
[44] West R N, Mayers J and Walters P A 1981 *J. Phys. E: Sci. Instrum.* **14** 478
Manuel A A, Samoilov S, Sachot R, Descouts P and Peter M 1979 *Solid State Commun.* **31** 955
Farmer W S, Sinclair F, Berko S and Beardsley G M 1979 *Solid State Commun.* **31** 481
[45] Cohen R E, Pickett W E, Boyer L L and Krakauer H 1988 *Phys. Rev. Lett.* **60** 817
Cohen R E, Pickett W E, Krakauer H and Boyer L L 1990 *Physica* B to be published
[46] Cava R J, Santoro A, Johnson D W Jr and Rhodes W W 1987 *Phys. Rev.* B **35** 6716
[47] Tanigawa S 1989 *Proc. 8th Int. Conf. on Positron Annihilation, Gent, Belgium 1988* to be published
[48] Chakraborty B 1981 *Phys. Rev.* B **24** 7423
Chakraborty B and Siegel R W 1983 *Phys. Rev.* B **27** 4535
Boronski E and Nieminen R M 1986 *Phys. Rev.* B **34** 3820
Jarlborg T and Singh A K 1987 *Phys. Rev.* B **36** 4660
[49] Wachs A L, Turchi P E A, Kaiser J H, West R N, Howell R H, Jean Y C, Merkle K L, Revcolevschi A and Fluss M J 1989 *Proc. 8th Int. Conf. on Positron Annihilation, Gent, Belgium, 1988*